Inorganic Chemistry
Article
pubs.acs.org/IC

Control of Bond-Strain-Induced Electronic Phase Transitions in Iron Perovskites

Ikuya Yamada,[*,‡,§,#] Hidenobu Etani,[§] Kazuki Tsuchida,[§] Shohei Marukawa,[⊥] Naoaki Hayashi,[∥] Takateru Kawakami,[↓] Masaichiro Mizumaki,[¶,⊕] Kenya Ohgushi,[•] Yoshihiro Kusano,[○] Jungeun Kim,[¶] Naruki Tsuji,[¶] Ryoji Takahashi,[§] Norimasa Nishiyama,[#,⧓,†] Toru Inoue,[⧓] Tetsuo Irifune,[⧓] and Mikio Takano[∥]

[‡]Nanoscience and Nanotechnology Research Center, Osaka Prefecture University, 1-2 Gakuen-cho, Naka-ku, Sakai, Osaka 599-8570, Japan

[§]Department of Chemistry, Graduate School of Science and Engineering, Ehime University, 2-5 Bunkyo-cho, Matsuyama, Ehime 790-8577, Japan

[#]Precursory Research for Embryonic Science and Technology (PRESTO), Japan Science and Technology Agency (JST), Chiyoda-ku, Tokyo 102-0075, Japan

[⊥]Department of Chemistry, Graduate School of Science, Osaka Prefecture University, 1-1 Gakuen-cho, Naka-ku, Sakai, Osaka 599-8531, Japan

[∥]Institute for Integrated Cell-Material Sciences (iCeMS), Kyoto University, Yoshidaushinomiya-cho, Sakyo-ku, Kyoto 606-8501, Japan

[↓]Department of Physics, College of Humanities and Sciences, Nihon University, Sakurajosui, Setagaya-ku, Tokyo 156-8550, Japan

[¶]Japan Synchrotron Radiation Research Institute (JASRI), Sayo-cho, Sayo-gun, Hyogo 679-5198, Japan

[⊕]Core Research for Evolutional Science and Technology (CREST), JST, 5 Sanbancho, Chiyoda-ku, Tokyo 102-0075, Japan

[•]Institute for Solid State Physics (ISSP), University of Tokyo, 5-1-5 Kashiwanoha, Kashiwa, Chiba 227-8581, Japan

[○]Department of Applied Arts and Design, Kurashiki University of Science and the Arts, 2640 Nishinoura, Tsurajima-cho, Kurashiki, Okayama 712-8505, Japan

[⧓]Geodynamics Research Center (GRC), Ehime University, 2-5 Bunkyo-cho, Matsuyama, Ehime 790-8577, Japan

Supporting Information

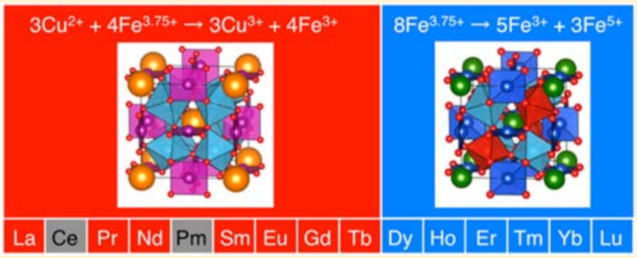

ABSTRACT: Unusual electronic phase transitions in the *A*-site ordered perovskites $LnCu_3Fe_4O_{12}$ (*Ln*: trivalent lanthanide ion) are investigated. All $LnCu_3Fe_4O_{12}$ compounds are in identical valence states of $Ln^{3+}Cu^{2+}{}_3Fe^{3.75+}{}_4O_{12}$ at high temperature. $LnCu_3Fe_4O_{12}$ with larger *Ln* ions (*Ln* = La, Pr, Nd, Sm, Eu, Gd, Tb) show an intersite charge transfer transition ($3Cu^{2+} + 4Fe^{3.75+} \rightarrow 3Cu^{3+} + 4Fe^{3+}$) in which the transition temperature decreases from 360 to 240 K with decreasing *Ln* ion size. In contrast, $LnCu_3Fe_4O_{12}$ with smaller *Ln* ions (*Ln* = Dy, Ho, Er, Tm Yb, Lu) transform into a charge-disproportionated ($8Fe^{3.75+} \rightarrow 5Fe^{3+} + 3Fe^{5+}$) and charge-ordered phase below ∼250−260 K. The former series exhibits metal-to-insulator, antiferromagnetic, and isostructural volume expansion transitions simultaneously with intersite charge transfer. The latter shows metal-to-semiconductor, ferrimagnetic, and structural phase transitions simultaneously with charge disproportionation. Bond valence calculation reveals that the metal−oxygen bond strains in these compounds are classified into two types: overbonding or compression stress (underbonding or tensile stress) in the *Ln*−O (Fe−O) bond is dominant in the former series, while the opposite stresses or bond strains are found in the latter. Intersite charge transfer transition temperatures are strongly dependent upon the global instability indices that represent the structural instability calculated from the bond valence sum, whereas the charge disproportionation occurs at almost identical temperatures, regardless of the magnitude of structural instability. These findings provide a new aspect of the structure−property relationship in transition metal oxides and enable precise control of electronic states by bond strains.

1. INTRODUCTION

Transition metal oxides have been extensively investigated because of a rich variety of interesting properties.[1] Together

Received: September 17, 2013
Published: November 13, 2013

dx.doi.org/10.1021/ic402344m | *Inorg. Chem.* 2013, 52, 13751−13761

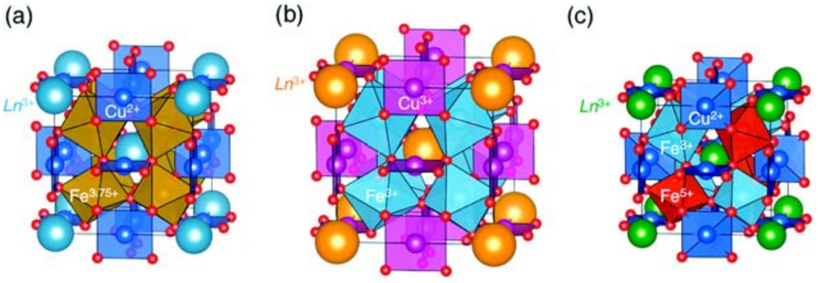

Figure 1. Various crystal structures and electronic states for $LnCu_3Fe_4O_{12}$ in the (a) high-temperature phase, $Ln^{3+}Cu^{2+}{}_3Fe^{3.75+}{}_4O_{12}$ (*Ln* = La−Lu); (b) low-temperature charge-transferred phase, $Ln^{3+}Cu^{3+}{}_3Fe^{3+}{}_4O_{12}$ (*Ln* = La, Pr, Nd, Sm, Eu, Gd, Tb); and (c) low-temperature charge-disproportionated and charge-ordered phase, $Ln^{3+}Cu^{2+}{}_3Fe^{3+}{}_2(Fe^{5+}{}_{3/4},Fe^{3+}{}_{1/4})_2O_{12}$ (*Ln* = Y, Dy, Ho, Er, Tm, Yb, Lu).

with nominal valence tuning using chemical substitutions and cation/anion vacancies, the adjustment of local structure such as metal−oxygen bond lengths and bond angles is a key element to achieve fascinating properties. Several kinds of indices are proposed for characterizing crystal structures of compounds. Brown's bond valence model[2,3] is widely used for estimating not only nominal valences but also the structural stability of certain compounds. The bond valence sum (BVS) is calculated from cation−anion bond lengths, and in normal cases, it matches the formal ionic valence. A difference between BVS and the ionic valence is called a bond discrepancy, which represents a steric bond strain, and their root-mean-square in the formula unit, global instability index (GII),[3] can be used to empirically evaluate structural instability.[4−6]

Iron-based perovskites $A^{2+}Fe^{4+}O_3$ (*A*: Ca, Sr, Ba), which include unusual high valence Fe^{4+} ions, are known to demonstrate versatile electronic properties with structural modifications. The simple cubic perovskite $SrFeO_3$ has a metallic conductivity down to low temperatures and displays complicated spin structures,[7−9] which are different from the isoelectronic Mn^{3+}-based perovskites with $3d^4$ electron configuration because of the difference in the charge transfer energy (energy for ligand-to-metal electron transfer), Δ_{CT}. The Δ_{CT} is positive for Mn^{3+} (+1.8 eV) and negative for Fe^{4+} (−3 eV).[10,11] This discriminative electronic state also induces intriguing phenomena in other $A^{2+}Fe^{4+}O_3$ perovskites, such as the charge disproportionation (CD) of $2Fe^{4+} \rightarrow Fe^{5+} + Fe^{3+}$ ($2Fe^{3+}\underline{L} \rightarrow Fe^{3+}\underline{L}^2 + Fe^{3+}$, $\underline{L}$: ligand hole) in the orthorhombic perovskite $CaFeO_3$ and the ferromagnetic alignment of Fe spins in the simple cubic perovskite $BaFeO_3$.[12−15]

The *A*-site ordered perovskites $AA'_3B_4O_{12}$, in which the original *A*-sites are divided into an icosahedral coordinated *A*-site and a pseudosquare coordinated *A*′-site (see Figure 1), have been extensively studied in recent years because of their fascinating structural and electronic features such as large magnetoresistance, giant dielectricity, heavy-fermion-like behavior, charge/orbital/spin-orderings, pressure-induced charge-disproportionation/ordering, and unusual high coordination.[16−22] In particular, Fe^{4+}-incorporated $ACu_3Fe_4O_{12}$ perovskites demonstrate highly intriguing phenomena due to their unusual electronic phase transitions. For instance, $Ca^{2+}Cu^{2+}{}_3Fe^{4+}{}_4O_{12}$ shows a charge disproportionation with a rock salt-type Fe^{3+}/Fe^{5+} charge ordering, a ferrimagnetic ordering of $Cu^{2+}\downarrow Fe^{5+}\uparrow Fe^{3+}\uparrow$, and a metal-to-semiconductor transition simultaneously at 210 K.[23] Instead, $Sr^{2+}Cu^{2+}{}_3Fe^{4+}{}_4O_{12}$, which contains a larger divalent cation at the *A*-site, displays a crossover-like intersite charge transfer featuring a negative thermal expansion between 170 and 270 K, followed by a charge disproportionation with a relative abundance of Fe^{5+}:Fe^{3+} of ∼1:4.[24] Such considerable dependence of structural and electronic properties upon *A*-site ion size was also reported for the $A^{3+}Cu^{2+}{}_3Fe^{3.75+}{}_4O_{12}$ perovskites. Figure 1 shows various crystal structures and electronic states for $A^{3+}Cu_3Fe_4O_{12}$ (*A* = La, Bi, Y).[25−27] All have an identical valence state of $A^{3+}Cu^{2+}{}_3Fe^{3.75+}{}_4O_{12}$ at high temperature, crystallizing into the cubic $AA'_3B_4O_{12}$-type perovskite with the space group $Im\overline{3}$ (No. 204) and with paramagnetic and metallic properties. Upon cooling to low temperature, the valence state transforms into two distinct states. $LaCu_3Fe_4O_{12}$ and $BiCu_3Fe_4O_{12}$ show an intersite charge transfer (CT) transition of $3Cu^{2+} + 4Fe^{3.75+} \rightarrow 3Cu^{3+} + 4Fe^{3+}$ below 393 K (La) and 428 K (Bi), respectively.[26,27] In contrast, $YCu_3Fe_4O_{12}$ shows a CD transition of $8Fe^{3.75+} \rightarrow 5Fe^{3+} + 3Fe^{5+}$ below 250 K,[25] which is similar to that of $CaCu_3Fe_4O_{12}$ rather than the CT transition of isoelectronic compounds. The resulting low-temperature phases in the $A^{3+}Cu_3Fe_4O_{12}$ perovskites have different crystal structures and physical properties. The $A^{3+}Cu^{3+}{}_3Fe^{3+}{}_4O_{12}$ (*A* = La, Bi) phase retains the $Im\overline{3}$ space group, but the $Y^{3+}Cu^{2+}{}_3(Fe^{3+},Fe^{5+})_4O_{12}$ phase has two crystallographic Fe sites for Fe^{3+} and $(Fe^{5+}{}_{3/4}Fe^{3+}{}_{1/4})$ ions because of charge ordering, lowering its symmetry to the space group $Pn\overline{3}$ (No. 201) (Figure 1). Although the former electronic phase displays an insulator-like electrical conductivity with a large temperature dependence and an antiferromagnetic ordering of Fe^{3+} spins, the latter shows a metal-to-semiconductor-like transition with slight temperature dependence and a ferrimagnetic ordering of Cu^{2+} and (Fe^{3+},Fe^{5+}) spins. It is notable that such a considerable dependence of the electronic phases upon *A*-site ion size has never been reported in isoelectronic $AA'_3B_4O_{12}$-type perovskites.[28,29] To unveil the origin of the difference between CT and CD transitions for $A^{3+}Cu_3Fe_4O_{12}$, we have performed structural analysis based on the bond valence models of $LaCu_3Fe_4O_{12}$ and $YCu_3Fe_4O_{12}$. In a previous paper,[25] we proposed that intolerable strains (compression or tensile stress) on *A*−O and Fe−O bonds, which are represented as an overbonding (underbonding) of *A*−O (Fe−O) bonds,[2,30] may become a driving force for CT, while the opposite type of bond strains do not induce a CT transition. However, the limited number of sample compounds could not allow us to conduct an in-depth study of the relationship between bond strains and electronic phases. In this paper, we show a systematic study of crystal structures, electronic states, and physical properties of $LnCu_3Fe_4O_{12}$ (*Ln*: lanthanide, La, Pr, Nd, Sm, Eu, Gd, Tb, Dy, Ho, Er, Tm, Yb, Lu), in which the *A*-site ion size may be precisely adjusted by lanthanide contraction from La^{3+} (Shannon's eight-coordinate ionic radius,[31] r_{La} = 1.16 Å) to Lu^{3+} (r_{Lu} = 0.977 Å), obtaining the whole electronic phase diagram of these compounds.

Careful analysis of bond strains leads to the conclusion that the electronic phase transition in $LnCu_3Fe_4O_{12}$ is controlled by subtle differences in the types of bond strains on Ln−O and Fe−O bonds.

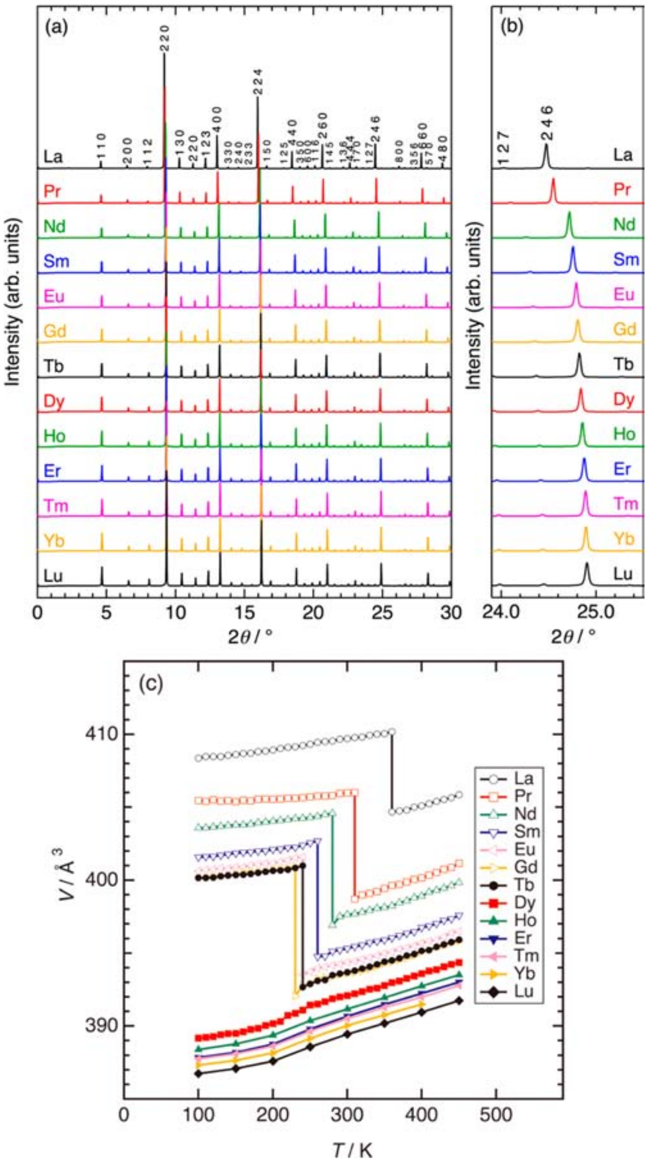

Figure 2. SXRD patterns for $LnCu_3Fe_4O_{12}$ in 2θ ranges (a) between 0 and 30° and (b) between 23.9 and 25.5° collected at 300 K. Selected *hkl* reflections are indexed. The wavelength was 0.42085 Å. (c) Temperature dependence of V for $LnCu_3Fe_4O_{12}$. The data for Ln = La, Pr, Nd, Sm, Eu, Gd, Tb, Dy are obtained from XRD, and for Ln = Dy, Ho, Er, Tm, Yb, Lu from SXRD.

2. EXPERIMENTAL SECTION

A precursor was prepared by the polymerized complex method[32] as in the synthesis of $YCu_3Fe_4O_{12}$.[25] Stoichiometric amounts of lanthanide oxides (99.9%), $Cu(NO_3)_2{\cdot}3H_2O$ (99.9%), and $Fe(NO_3)_3{\cdot}9H_2O$ (99.9%) were dissolved in nitric acid, to which a 5-fold excess of citric acid and a one-fold excess of 1,2-ethanediol were added while stirring. The resulting solution was heated, while being stirred, up to 573 K and kept there for 1 h to dryness. Subsequently, the dried powder was fired using a furnace at 673 K for 1 h and 948 K for 12 h in air with occasional grindings. The obtained precursor with a nominal chemical composition of $LnCu_3Fe_4O_{10.5}$ was mixed with an oxidizing agent $KClO_4$ (99.9%) in a molar ratio of 2:1. The sample mixture was sealed off during the treatment in a platinum capsule with an inner diameter of 2.3−2.8 mm and a height of 4.0 mm. The capsule was placed into a (Mg,Co)O pressure medium, and compressed to 15 GPa using a high-pressure apparatus. The sample was subsequently heated to 1273−1473 K in 20 min, kept at this temperature for 30 min, and quenched to room temperature. The pressure was slowly released after the heat treatment. The obtained polycrystalline sample was washed several times with water, ethanol, and acetone.

The synchrotron X-ray powder diffraction (SXRD) experiments were performed at the BL02B2 beamline of SPring-8, Japan, using samples contained in Lindemann glass capillary tubes with an inner diameter of 0.2 mm. The wavelength used was determined to be 0.42085 Å using a CeO_2 standard. Structure parameters were refined by Rietveld analysis using the program RIETAN-FP.[33] The crystal structures were drawn using the VESTA software.[34] An absorption correction was not considered in the refinement because the absorption effect was expected to be negligibly small. Electron diffraction (ED) patterns of $LuCu_3Fe_4O_{12}$ were collected at 300 and 200 K using a transmission electron microscope (TOPCON, EM-002B).

The ^{57}Fe Mössbauer spectroscopy measurements were performed for selected samples of $LnCu_3Fe_4O_{12}$ (Ln = Eu, Tb, Dy, Lu) in transmission geometry using ^{57}Co/Rh as a radiation source and α-Fe as a control for velocity calibration and isomer shift. Collected Mössbauer spectra were fitted computationally using the Lorentzian function. Soft X-ray absorption spectroscopy (XAS) and magnetic circular dichroism (MCD) for the Cu $L_{2,3}$- and Fe $L_{2,3}$-edges were measured at 15 K in an external magnetic field of 19 kOe using a total electron yield method at the BL25SU and BL27SU beamlines of SPring-8. Magnetization measurements were conducted using a superconducting quantum interference device (SQUID, Quantum Design MPMS-XL) between 5 and 400 K under external fields up to 50 kOe. Electrical resistivity was measured by the standard four-probe method using a Quantum Design Physical Properties Measurement System (PPMS).

3. RESULTS AND DISCUSSION

We successfully obtained high-quality samples of $LnCu_3Fe_4O_{12}$ (Ln = Pr, Nd, Sm, Eu, Gd, Tb, Dy, Ho, Er, Tm, Yb, Lu), and using X-ray diffractometry we were able to split them into two classes. Figure 2a shows the SXRD patterns for $LnCu_3Fe_4O_{12}$ at 300 K. The primary phase for all of the compounds is the cubic $AA'_3B_4O_{12}$-type perovskite (space group $Im\overline{3}$, No. 204) with a lattice constant a = 7.303−7.429 Å. All are single-phase or contain a very small amount of impurity phase(s) (presumably, up to a few wt %). Figure 2b shows the SXRD patterns for $LnCu_3Fe_4O_{12}$ near the 2 4 6 Bragg reflection. The 2 4 6 peak monotonically shifts to higher angle with decreasing r_{Ln}, corresponding to a unit cell volume shrinkage from ∼410 Å^3 for $LaCu_3Fe_4O_{12}$ to ∼390 Å^3 for $LuCu_3Fe_4O_{12}$ at this temperature. Figure 2c shows the temperature dependence of the unit cell volume, V, for $LnCu_3Fe_4O_{12}$. An abrupt volume change is observed in $LaCu_3Fe_4O_{12}$ at 360 K, which is attributed to the CT transition, as previously reported.[26] Similar anomalies observed in $LnCu_3Fe_4O_{12}$ with larger Ln ions (Ln = Pr, Nd, Sm, Eu, Gd, Tb) at temperatures between 230 and 320 K may also be attributed to CT transitions (see also the XRD patterns collected in a temperature range of 100−450 K shown in Figure S1 in the Supporting Information [SI]). Note that the CT transition temperatures tend to lower with decreasing r_{Ln}. On the other hand, $LnCu_3Fe_4O_{12}$ with smaller Ln ions (Ln = Dy, Ho, Er, Tm, Yb, Lu) display no clear anomaly between 100 and 450 K, implying an absence of CT transitions.

The valence states of the $LnCu_3Fe_4O_{12}$ were investigated using the bond valence method.[2] Rietveld refinement was conducted based on the SXRD data at temperatures between

Table 1. Refined Structure Parameters, Selected Bond Lengths (Å) and Angles (deg), and Bond Valence Sums for $Ln\mathrm{Cu_3Fe_4O_{12}}$ at 300 K[a]

Ln	La	Pr	Nd	Sm	Eu	Gd	Tb	Dy	Ho	Er	Tm	Yb	Lu
space group	$Im\bar{3}$	$Im\bar{3}$	$Im\bar{3}$	$Im\bar{3}$	$Im\bar{3}$	$Im\bar{3}$	$Im\bar{3}$	$Im\bar{3}$	$Im\bar{3}$	$Im\bar{3}$	$Im\bar{3}$	$Im\bar{3}$	$Im\bar{3}$
a (Å)	7.42874(6)	7.40361(7)	7.34783(6)	7.33892(6)	7.33641(8)	7.33184(9)	7.32212(6)	7.31441(5)	7.31337(6)	7.31041(6)	7.30930(7)	7.30638(6)	7.30335(6)
y (O)	0.3109(3)	0.3092(3)	0.3038(3)	0.3029(3)	0.3035(3)	0.3023(3)	0.3010(3)	0.3013(3)	0.3013(3)	0.3014(3)	0.2999(3)	0.2999(3)	0.3000(3)
z (O)	0.1701(3)	0.1692(4)	0.1766(3)	0.1755(3)	0.1760(3)	0.1753(3)	0.1746(3)	0.1753(3)	0.1751(3)	0.1746(3)	0.1738(3)	0.1747(3)	0.1747(3)
$U_{\mathrm{iso}}(Ln) \times 1000$ (Å^2)	2.61(14)	3.33(14)	2.76(14)	3.25(13)	4.06(13)	3.87(13)	3.65(11)	4.24(11)	4.92(11)	5.38(12)	5.56(12)	6.22(11)	6.99(11)
$U_{\mathrm{iso}}(\mathrm{Cu}) \times 1000$ (Å^2)	6.01(15)	5.78(16)	6.45(16)	6.43(15)	6.80(16)	5.68(15)	6.66(14)	5.68(14)	5.79(14)	5.67(14)	5.78(15)	5.71(14)	5.66(13)
$U_{\mathrm{iso}}(\mathrm{Fe}) \times 1000$ (Å^2)	3.58(13)	3.61(14)	3.07(14)	3.01(14)	3.18(14)	2.79(13)	3.07(12)	3.02(12)	2.86(12)	2.95(13)	2.97(13)	3.21(12)	2.92(12)
$U_{\mathrm{iso}}(\mathrm{O}) \times 1000$ (Å^2)	3.5(6)	3.9(6)	5.7(7)	5.3(6)	5.6(7)	5.0(6)	5.8(6)	6.6(6)	6.0(6)	5.6(6)	4.8(7)	6.5(6)	4.8(6)
Ln−O (× 12) (Å)	2.633(2)	2.610(3)	2.579(3)	2.569(2)	2.574(2)	2.563(2)	2.548(2)	2.550(2)	2.548(2)	2.547(2)	2.534(2)	2.536(2)	2.5354(19)
Cu−O (× 4) (Å)	1.889(2)	1.888(2)	1.935(2)	1.937(2)	1.935(2)	1.937(2)	1.939(2)	1.938(2)	1.937(2)	1.933(2)	1.938(2)	1.941(2)	1.9397(19)
Cu−O (× 4) (Å)	2.825(2)	2.827(3)	2.785(3)	2.786(3)	2.780(3)	2.787(2)	2.793(2)	2.785(2)	2.785(2)	2.787(2)	2.797(2)	2.791(2)	2.789(2)
Fe−O (× 6) (Å)	2.0016(8)	1.9939(9)	1.9566(8)	1.9535(8)	1.9527(8)	1.9510(7)	1.9480(7)	1.9451(7)	1.9450(7)	1.9456(7)	1.9448(8)	1.9421(7)	1.9414(7)
Fe−O−Fe (deg)	136.20(12)	136.33(13)	139.71(13)	139.84(13)	139.86(13)	139.92(12)	140.00(11)	140.15(12)	140.10(12)	139.89(12)	139.98(13)	140.28(12)	140.26(11)
BVS(Ln) (v.u.)[b]	3.46	3.32	3.44	3.27	3.13	3.13	3.11	3.00	2.90	2.81	2.84	2.71	2.61
BVS(Cu) (v.u.)[b]	2.88	2.89	2.03	2.02	2.03	2.02	2.01	2.02	2.02	2.04	2.01	2.00	2.01
BVS(Fe) (v.u.)[b]	3.05	3.11	3.64	3.67	3.68	3.70	3.73	3.76	3.76	3.75	3.76	3.79	3.80
R_{wp} (%)	7.166	7.315	6.549	6.893	6.522	5.657	6.175	5.832	5..892	5.743	6.660	5.929	5.312
R_{B} (%)	1.372	1.362	1.829	1.375	1.992	1.703	1.028	1.039	1.440	1.883	1.435	1.339	1.245
GOF	1.0522	1.0636	1.0819	1.0763	1.0509	0.9679	0.9539	0.9285	0.9238	0.9938	1.0662	0.9766	0.8868

[a] Atomic sites: Ln 2a (0, 0, 0), Cu 6b (0, $^1/_2$, $^1/_2$), Fe 8c ($^1/_4$, $^1/_4$, $^1/_4$), O 24g (0, y, z). The occupancy factor g for all sites was fixed at unity. [b] The BVS were calculated using the following parameters: b_0 = 0.37 for all atoms, r_0 = 2.172 for La^{3+}, r_0 = 2.135 for Pr^{3+}, r_0 = 2.117 for Nd^{3+}, r_0 = 2.088 for Sm^{3+}, r_0 = 2.076 for Eu^{3+}, r_0 = 2.065 for Gd^{3+}, r_0 = 2.049 for Tb^{3+}, r_0 = 2.036 for Dy^{3+}, r_0 = 2.023 for Ho^{3+}, r_0 = 2.010 for Er^{3+}, r_0 = 2.000 for Tm^{3+}, r_0 = 1.985 for Yb^{3+}, r_0 = 1.971 for Lu^{3+}, r_0 = 1.649 for Cu^{2+}, r_0 = 1.739 for Cu^{3+}, r_0 = 1.751 for Fe^{3+}, and r_0 = 1.772 for Fe$^{3.75+}$.[40,41]

Table 2. Refined Structure Parameters, Selected Bond Lengths and Angles, and Bond Valence Sums for $Ln\text{Cu}_3\text{Fe}_4\text{O}_{12}$ at 100 K[a]

Ln	La	Pr	Nd	Sm	Eu	Gd	Tb	Dy	Ho	Er	Tm	Yb	Lu
space group	$Im\bar{3}$	$Im\bar{3}$	$Im\bar{3}$	$Im\bar{3}$	$Im\bar{3}$	$Im\bar{3}$	$Im\bar{3}$	$Pn\bar{3}$	$Pn\bar{3}$	$Pn\bar{3}$	$Pn\bar{3}$	$Pn\bar{3}$	$Pn\bar{3}$
a (Å)	742008(6)	7.39474(7)	7.38247(6)	7.37561(6)	7.37306(8)	7.37144(9)	7.36687(8)	7.29665(5)	7.29610(6)	7.29271(6)	7.29208(7)	7.28933(6)	7.28577(6)
x (O)	0	0	0	0	0	0	0	0.247(2)	0.2458(14)	0.248(3)	0.249(6)	0.247(2)	0.248(3)
y (O)	0.3108(3)	0.3094(3)	0.3087(3)	0.3078(3)	0.3082(3)	0.3074(3)	0.3080(3)	0.4257(3)	0.4252(3)	0.4250(3)	0.4250(3)	0.4248(3)	0.4252(3)
z (O)	0.1699(3)	0.1693(4)	0.1690(4)	0.1684(3)	0.1687(4)	0.1682(3)	0.1684(3)	0.5511(3)	0.5506(3)	0.5509(3)	0.5495(3)	0.5496(3)	0.5496(3)
$U_{\text{iso}}(Ln) \times 1000$ (Å^2)	0.49(12)	0.80(13)	0.63(13)	1.16(12)	1.87(13)	1.77(5)	2.38(6)	1.24(3)	1.45(3)	1.95(10)	1.94(11)	2.10(10)	2.81(9)
$U_{\text{iso}}(\text{Cu}) \times 1000$ (Å^2)	3.99(13)	3.48(15)	3.27(15)	3.42(14)	3.69(16)	2.86(8)	2.41(8)	3.07(4)	2.97(3)	2.85(13)	3.23(14)	2.99(13)	3.22(11)
$U_{\text{iso}}(\text{Fe1}) \times 1000$ (Å^2)	1.68(12)	1.68(13)	1.46(13)	1.52(13)	1.66(14)	1.59(4)	1.11(4)	1.44(3)[b]	1.32(2)[b]	1.26(12)[b]	1.35(13)[b]	1.37(12)[b]	1.33(10)[b]
$U_{\text{iso}}(\text{Fe2}) \times 1000$ (Å^2)	–	–	–	–	–	–	–	1.44(3)[b]	1.32(2)[b]	1.26(12)[b]	1.35(13)[b]	1.37(12)[b]	1.33(10)[b]
$U_{\text{iso}}(\text{O}) \times 1000$ (Å^2)	1.4(5)	2.4(6)	2.7(6)	2.0(6)	2.3(7)	2.23(11)	2.12(11)	3.58(10)	3.24(8)	2.8(7)	3.6(7)	3.7(7)	2.8(6)
Ln–O (× 12) (Å)	2.628(2)	2.608(3)	2.598(3)	2.588(2)	2.591(3)	2.583(2)	2.586(2)	2.544(2)	2.539(2)	2.539(2)	2.529(2)	2.528(2)	2.5289(19)
Cu–O (× 4) (Å)	1.887(2)	1.885(2)	1.885(2)	1.885(2)	1.884(3)	1.884(2)	1.882(2)	1.936(2)	1.937(2)	1.934(2)	1.941(2)	1.939(2)	1.9391(19)
Cu–O (× 4) (Å)	2.824(30	2.823(3)	2.823(3)	2.827(3)	2.822(3)	2.828(2)	2.883(2)	2.776(2)	2.781(2)	2.779(2)	2.785(2)	2.785(2)	2.781(2)
Fe1–O (× 6) (Å)	1.9995(8)	1.9916(9)	1.9879(9)	1.9859(9)	1.9851(9)	1.9848(8)	1.9839(8)	1.957(17)	1.969(10)	1.96(2)	1.95(4)	1.959(15)	1.95(2)
Fe2–O (× 6) (Å)	–	–	–	–	–	–	–	1.921(17)	1.910(10)	1.92(2)	1.93(4)	1.915(15)	1.92(2)
Fe–O–Fe (deg)	136.17(12)	136.32(13)	136.38(13)	136.41(12)	136.42(14)	136.40(11)	136.35(11)	140.32(12)	140.25(11)	140.16(12)	140.46(13)	140.36(13)	140.49(11)
BVS(Ln) (v.u.)	3.50	3.34	3.27	3.11	2.99	2.96	2.81	3.04	2.98	2.88	2.87	2.76	2.66
BVS(Cu) (v.u.)	2.90	2.91	2.91	2.91	2.92	2.91	2.94	2.03	2.03	2.04	2.00	2.01	2.01
BVS(Fe1) (v.u.)	3.07	3.13	3.16	3.18	3.19	3.19	3.20	3.44	3.33	3.46	3.55	3.42	3.52
BVS(Fe2) (v.u.)	–	–	–	–	–	–	–	3.95[c]	4.07[c]	3.93[c]	3.87[c]	4.02[c]	3.95[c]
R_{wp} (%)	6.981	7.357	6.724	6.919	6.943	5.492	5.489	5.934	5.531	5.723	6.866	6.319	5.346
R_{B} (%)	1.172	1.250	1.820	1.052	1.455	1.105	1.275	0.957	1.146	1.436	1.264	0.814	1.047
GOF	1.0162	1.0585	1.1132	1.0640	1.1247	0.9849	0.9567	0.9518	0.8853	0.9914	1.1081	1.0326	0.9012

[a] Atomic sites: Ln $2a$ (0, 0, 0), Cu $6b$ (0, $^1/_2$, $^1/_2$), Fe $8c$ ($^1/_4$, $^1/_4$, $^1/_4$), O $24g$ (0, y, z) for $\text{Im}\bar{3}$ (No. 204); Ln $2a$ ($^1/_4$, $^1/_4$, $^1/_4$), Cu $6d$ ($^1/_4$, $^3/_4$, $^3/_4$), Fe1 $4b$ (0, 0, 0), Fe2 $4c$ ($^1/_2$, $^1/_2$, $^1/_2$), O $24h$ (x, y, z) for $Pn\bar{3}$ (No. 201); The occupancy factor g for all sites was fixed at unity. [b] The following constraint was adopted: $U_{\text{iso}}(\text{Fe1}) = U_{\text{iso}}(\text{Fe2})$. The BVS were calculated using the following parameters: $b_0 = 0.37$ for all atoms, $r_0 = 2.172$ for La^{3+}, $r_0 = 2.135$ for Pr^{3+}, $r_0 = 2.117$ for Nd^{3+}, $r_0 = 2.088$ for Sm^{3+}, $r_0 = 2.076$ for Eu^{3+}, $r_0 = 2.065$ for Gd^{3+}, $r_0 = 2.049$ for Tb^{3+}, $r_0 = 2.036$ for Dy^{3+}, $r_0 = 2.023$ for Ho^{3+}, $r_0 = 2.010$ for Er^{3+}, $r_0 = 2.000$ for Tm^{3+}, $r_0 = 1.985$ for Yb^{3+}, $r_0 = 1.971$ for Lu^{3+}, $r_0 = 1.649$ for Cu^{2+}, $r_0 = 1.739$ for Cu^{3+}, $r_0 = 1.751$ for Fe^{3+}, and $r_0 = 1.772$ for Fe^{5+}.[40,41] [c] The BVS of the Fe2 site was calculated as follows: BVS(Fe2) = $^3/_4$BVS(Fe^{5+}, $r_0 = 1.772$) + $^1/_4$BVS(Fe^{3+}, $r_0 = 1.751$).

100 and 450 K. Table 1 lists the structure parameters obtained from Rietveld refinement for the data at 300 K (also see the SXRD profiles and the fitting results in Figure S2 of the SI). A stoichiometric model was adopted for simplicity because structural disorders in these compounds were expected to be insignificant, although a few atom % of Fe ions incorporated into the Cu sites were confirmed by Mössbauer spectroscopy (shown later). The Rietveld refinement at this temperature gave excellent reliability factors and a goodness of fit (GOF), showing $R_{wp} < 8\%$, $R_B < 2\%$, and GOF < 1.1. The BVS values of *Ln*, Cu, and Fe ions for $Ln\text{Cu}_3\text{Fe}_4\text{O}_{12}$ (*Ln* = Nd, Sm, Eu, Gd, Tb, Dy, Ho, Er, Tm, Yb, Lu) are 2.61−3.44, 2.00−2.03, 3.64−3.80, respectively, which are close to +3, +2, and +3.75 at this temperature, respectively. This reflects that these compounds have $Ln^{3+}\text{Cu}^{2+}{}_3\text{Fe}^{3.75+}{}_4\text{O}_{12}$ valence states (see Table 1), while the BVS values of *Ln*, Cu, and Fe ions for $\text{LaCu}_3\text{Fe}_4\text{O}_{12}$ and $\text{PrCu}_3\text{Fe}_4\text{O}_{12}$ are 3.32−3.46, 2.88−2.89, and 3.05−3.11, respectively, suggesting that their appropriate ionic models are $Ln^{3+}\text{Cu}^{3+}{}_3\text{Fe}^{3+}{}_4\text{O}_{12}$. The SXRD patterns at 100 K were indexed in the cubic $AA'_3B_4\text{O}_{12}$-type perovskite structure for all. Several compounds (*Ln* = Gd, Tb, Dy, Ho) contained very small amounts (1−3%) of isostructural secondary phases. These phases are presumably attributed to off-stoichiometry and/or crystallites strained by external stress, which may unexpectedly give rise to other types of phase transitions, and therefore we exclude secondary phases from the discussion. Table 2 lists the structure parameters obtained from Rietveld refinement for the data at 100 K (see also the SXRD profiles and the fitting results in Figure S3 in the SI). The SXRD data of $Ln\text{Cu}_3\text{Fe}_4\text{O}_{12}$ (*Ln* = La, Pr, Nd, Sm, Eu, Gd, Tb) were refined based on the $Im\overline{3}$ space group. The BVS values of *Ln*, Cu, and Fe ions for these compounds are 2.96−3.50, 2.90−2.92, and 3.07−3.19, respectively, all of which are close to +3, confirming that the $Ln^{3+}\text{Cu}^{3+}{}_3\text{Fe}^{3+}{}_4\text{O}_{12}$ valence states are appropriate. These results allow us to conclude that the volume expansions are associated with CT transitions of $3\text{Cu}^{2+} + 4\text{Fe}^{3.75+} \rightarrow 3\text{Cu}^{3+} + 4\text{Fe}^{3+}$. The ED data of $\text{LuCu}_3\text{Fe}_4\text{O}_{12}$ displayed a symmetry lowering from $Im\overline{3}$ at 300K to $Pn\overline{3}$ (No. 201) at 200 K (see Figure S4 in the SI). This implies a charge ordering of Fe^{3+} and ($\text{Fe}^{5+}{}_{3/4}$, $\text{Fe}^{3+}{}_{1/4}$) ions in the charge-disproportionated phase, as reported previously in $\text{YCu}_3\text{Fe}_4\text{O}_{12}$.[25] Hence, we made structure refinement using the SXRD data of $\text{LuCu}_3\text{Fe}_4\text{O}_{12}$ at 100 K in the $Pn\overline{3}$ space group, obtaining a reliable charge-ordered structure (Table 2 and Figure S3 in the SI). Also the SXRD data of $Ln\text{Cu}_3\text{Fe}_4\text{O}_{12}$ (*Ln* = Dy, Ho, Er, Tm, Yb) at 100 K could be reasonably refined in the $Pn\overline{3}$ space group, showing two distinct Fe−O bond lengths for the charge-ordered structure. Therefore, we conclude that CD phase transitions ($8\text{Fe}^{3.75+} \rightarrow 5\text{Fe}^{3+} + 3\text{Fe}^{5+}$) occur at low temperatures between 100 and 300 K for the $Ln\text{Cu}_3\text{Fe}_4\text{O}_{12}$ with smaller *Ln* ions (*Ln* = Dy, Ho, Er, Tm, Yb, Lu) instead of CT transitions.

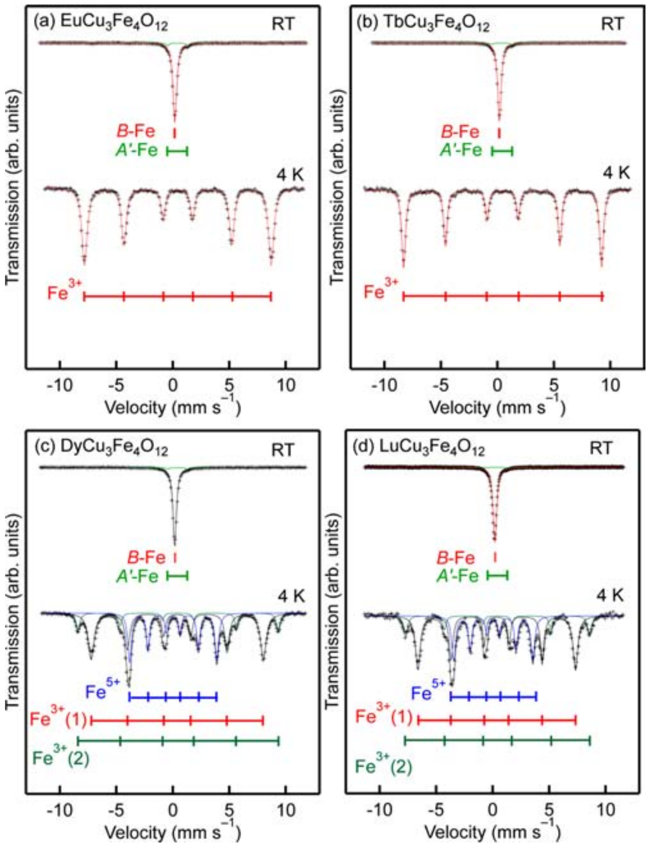

Figure 3. Mössbauer spectra of $Ln\text{Cu}_3\text{Fe}_4\text{O}_{12}$ measured at 4 K and room temperature; *Ln* = (a) Eu, (b) Tb, (c) Dy, (d) Lu.

The ^{57}Fe Mössbauer spectroscopy data confirmed the above-mentioned structure analysis results. Figure 3 shows Mössbauer spectra for selected $Ln\text{Cu}_3\text{Fe}_4\text{O}_{12}$ compounds (*Ln* = Eu, Tb, Dy, Lu) at 4 K and at room temperature, and their hyperfine parameters are listed in Table 3. For all of the compounds, a primary component is a singlet with an isomer shift (*IS*) of 0.16−0.18 mm s^{-1} at room temperature. These *IS* values are similar to that reported for $\text{Y}^{3+}\text{Cu}^{2+}{}_3\text{Fe}^{3.75+}{}_4\text{O}_{12}$ (*IS* = 0.16 mm s^{-1} at 290 K)[25] rather than $\text{La}^{3+}\text{Cu}^{3+}{}_3\text{Fe}^{3+}{}_4\text{O}_{12}$ (*IS* = 0.34 mm s^{-1} at 298 K),[26] thus the iron valence is close to +3.75 at this temperature for all. A few % of Fe^{3+} ions are incorporated into the *A*′-site as a doublet with a large quadrupole splitting of ΔE_q ∼1.8 mm s^{-1}, as reported for $A\text{Cu}_3\text{Fe}_4\text{O}_{12}$ compounds (*A* = Ca, Sr, Y).[23−25] For $\text{EuCu}_3\text{Fe}_4\text{O}_{12}$ and $\text{TbCu}_3\text{Fe}_4\text{O}_{12}$, the primary singlet component transforms into a magnetic sextet with *IS* = ∼0.45 mm s^{-1} in the 4 K spectra. These *IS* values are close to that of $\text{LaCu}_3\text{Fe}_4\text{O}_{12}$ at the lowest temperature (0.47 mm s^{-1}),[35] verifying that the Fe^{3+} species are generated by CT transitions in $\text{EuCu}_3\text{Fe}_4\text{O}_{12}$ and $\text{TbCu}_3\text{Fe}_4\text{O}_{12}$. This fact allows us to conclude that the Fe^{3+} valence state is dominant in the low-temperature phases of $Ln\text{Cu}_3\text{Fe}_4\text{O}_{12}$ (*Ln* = Pr, Nd, Sm, Gd). For $\text{DyCu}_3\text{Fe}_4\text{O}_{12}$ and $\text{LuCu}_3\text{Fe}_4\text{O}_{12}$, on the other hand, the primary singlet component splits into three magnetic sextets (Fe^{5+}, Fe^{3+}(1), and Fe^{3+}(2)) in a ratio of Fe^{5+}:Fe^{3+}(1,2) = 3:5 at 4 K. These transformations are almost identical to that of $\text{YCu}_3\text{Fe}_4\text{O}_{12}$,[25] supporting the postulate that CD transitions of $8\text{Fe}^{3.75+} \rightarrow 5\text{Fe}^{3+} + 3\text{Fe}^{5+}$ occur in these compounds. Similar structural and electronic properties (shown later) observed in the intermediate compounds $Ln\text{Cu}_3\text{Fe}_4\text{O}_{12}$ (*Ln* = Ho, Er, Tm, Yb) indicate that these compounds also transform to the same electronic states at low temperature. Thus, we confirm that the electronic phase boundary between CT and CD phases is between $\text{TbCu}_3\text{Fe}_4\text{O}_{12}$ and $\text{DyCu}_3\text{Fe}_4\text{O}_{12}$.

The valence changes of Cu ions were confirmed by XAS. Figure 4a shows Cu-L_3 XAS spectra for $Ln\text{Cu}_3\text{Fe}_4\text{O}_{12}$ (*Ln* = La, Pr, Nd, Sm, Eu, Gd, Tb, Dy) collected at 300 K. The XAS spectral shape of $\text{LaCu}_3\text{Fe}_4\text{O}_{12}$ at 300 K, in which the two main peaks are located at ∼930.5 and ∼932.5 eV, is similar to that of $\text{LaCu}^{3+}\text{O}_3$,[36] while the single peak at ∼930.5 eV observed in $Ln\text{Cu}_3\text{Fe}_4\text{O}_{12}$ (*Ln* = Sm, Eu, Gd, Tb, Dy) at 300 K is similar to those of Cu^{2+}-oxides.[37] For $\text{PrCu}_3\text{Fe}_4\text{O}_{12}$, the XAS spectrum has a complicated structure because of overlapping Pr-M_5 absorption. We can see shoulder peaks at ∼932.5 eV in

Table 3. Hyperfine Parameters for $LnCu_3Fe_4O_{12}$ (*Ln* = Eu, Tb, Dy, and Lu) at Room Temperature (RT) and 4 K Deduced from Mössbauer Spectra

		$EuCu_3Fe_4O_{12}$	$TbCu_3Fe_4O_{12}$	$DyCu_3Fe_4O_{12}$	$LuCu_3Fe_4O_{12}$
			RT		
(1) *B*-Fe	IS/mm s^{-1}	0.18	0.18	0.17	0.16
	HF/kOe	0	0	0	0
	ΔE_q/mm s^{-1}	0	0	0	0
	atomic ratio (%)	95	97	96	99
(2) *A*′-Fe	IS/mm s^{-1}	0.42	0.39	0.42	0.38
	HF/kOe	0	0	0	0
	ΔE_q/mm s^{-1}	1.77	1.77	1.78	1.71
	atomic ratio (%)	5	3	4	1
			4 K		
(1) Fe^{3+}	IS/mm s^{-1}	0.45	0.46	0.39	0.36
	HF/kOe	513	543	473	432
	ΔE_q/mm s^{-1}	0	0	0	0
	atomic ratio (%)	100	100	52	51
(2) Fe^{3+}	IS/mm s^{-1}	–	–	0.47	0.44
	HF/kOe	–	–	550	504
	ΔE_q/mm s^{-1}	–	–	0	0
	atomic ratio (%)	–	–	13	14
(3) Fe^{5+}	IS/mm s^{-1}	–	–	0.03	0.05
	HF/kOe	–	–	239	217
	ΔE_q/mm s^{-1}	–	–	0	0
	atomic ratio (%)	–	–	35	35

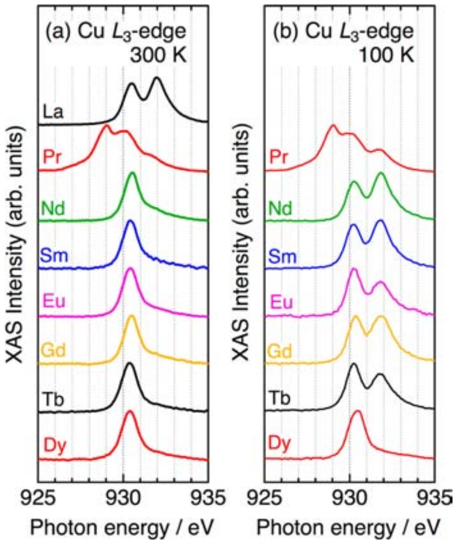

Figure 4. XAS spectra of Cu-L_3 edge for $LnCu_3Fe_4O_{12}$ (*Ln* = La, Pr, Nd, Sm, Eu, Gd, Tb, Dy) collected at (a) 300 K and (b) 100 K.

$PrCu_3Fe_4O_{12}$ and $NdCu_3Fe_4O_{12}$ XAS data, in addition to the main peak at ~930.5 eV. These shoulder peaks derive from a certain fraction of Cu^{3+} ions in these compounds because of the coexistence of $Ln^{3+}Cu^{2+}{}_3Fe^{3.75+}{}_4O_{12}$ and $Ln^{3+}Cu^{3+}{}_3Fe^{3+}{}_4O_{12}$ phases, as displayed in the XRD patterns (see Figure S2 in the SI). The XAS spectra of $LnCu_3Fe_4O_{12}$ (*Ln* = Pr, Nd, Sm, Eu, Gd, Tb) at 100 K show double peaks at ~930.5 and ~932.5 eV (see Figure 4b). This confirms that the Cu^{3+} valence states are dominant in these compounds. On the other hand, the XAS spectral shape of $DyCu_3Fe_4O_{12}$ is unchanged down to 100 K, exhibiting that the Cu^{2+} valence state is retained at this temperature. These results demonstrate that the Cu valence changes from divalent to trivalent at the CT transition for $LnCu_3Fe_4O_{12}$ (*Ln* = La, Pr, Nd, Sm, Eu, Gd, Tb), whereas the Cu^{2+} state is maintained for the charge-disproportionated $DyCu_3Fe_4O_{12}$ phase.

Figure 5a shows the temperature dependence of the magnetic susceptibility for $LnCu_3Fe_4O_{12}$. For $LnCu_3Fe_4O_{12}$ (*Ln* = La, Pr, Nd, Sm, Eu, Gd, Tb), antiferromagnetic transitions are observed. The Néel temperature (T_N) systematically decreases from 367 K (La) to 233 K (Tb) with decreasing r_{Ln}, which corresponds to the evolution of the CT transition temperature as shown in the XRD data (Figure 2c). On the other hand, $LnCu_3Fe_4O_{12}$ (*Ln* = Dy, Ho, Er, Tm, Yb, Lu) exhibit ferromagnetic transitions at almost identical Curie temperatures (T_C) of ~250–260 K. These values are close to T_C = ~250 K for $YCu_3Fe_4O_{12}$.[25] The susceptibility is slightly suppressed down to the lowest temperature for $LnCu_3Fe_4O_{12}$ (*Ln* = Dy, Ho, Er), which most likely originates from the 4f magnetic moments of the *Ln* ions making an antiparallel alignment with the Fe spins in low magnetic fields, in analogy with magnetic structures of ferrimagnetic $LnCu_3Mn_4O_{12}$ compounds.[29] Figure 5b displays the isothermal magnetization for $LnCu_3Fe_4O_{12}$ measured at 5 K. The antiferromagnetic compounds (*Ln* = La, Pr, Nd, Sm, Eu, Gd, Tb) show no sign of spontaneous magnetization, whereas the ferromagnetic compounds (*Ln* = Dy, Ho, Er, Tm, Yb, Lu) exhibit soft ferromagnetic behavior. $LuCu_3Fe_4O_{12}$ has no 4f magnetic moment because of the $4f^{14}$ electron configuration, displaying a saturation magnetization of ~7.6 μ_B per formula unit. This value is identical to that of $YCu_3Fe_4O_{12}$ (7.6 μ_B),[25] suggesting that $LuCu_3Fe_4O_{12}$ has the same magnetic structure (ferrimagnetic, $Cu^{2+}\downarrow$-$Fe^{5+}\uparrow$-$Fe^{3+}(1)\uparrow$-$Fe^{3+}(2)\downarrow$) as $YCu_3Fe_4O_{12}$. For other ferromagnetic compounds (*Ln* = Dy, Ho, Er, Tm, Yb), magnetization curves are complicated because of the contribution of the 4f magnetic moments. However, since antiparallel couplings between Cu and Fe are confirmed in MCD spectra (Figure S5 in the SI), their magnetic structures as concerns the Cu and Fe spins are considered to be identical to that of $LuCu_3Fe_4O_{12}$.

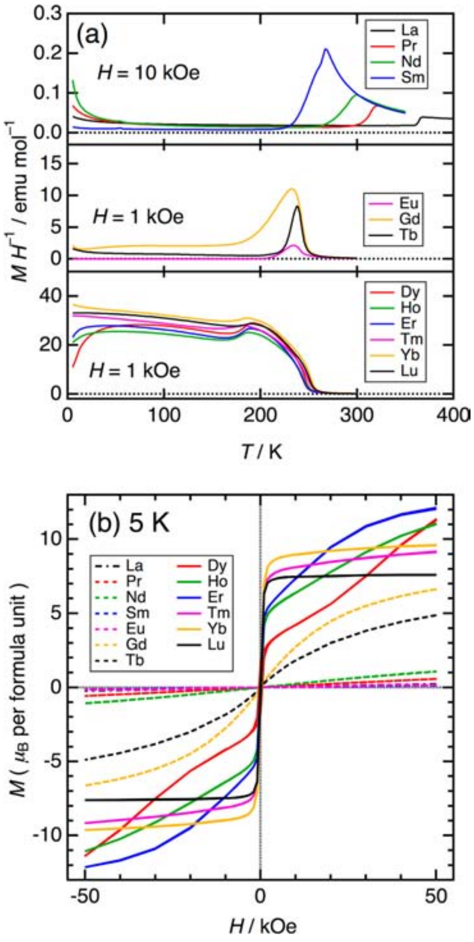

Figure 5. (a) Temperature dependence of the magnetic susceptibility for LnCu$_3$Fe$_4$O$_{12}$ on ZFC mode. Applied external field was 1 kOe (Ln = Sm, Eu, Gd, Tb, Dy, Ho, Er, Tm, Yb, Lu) and 10 kOe (Ln = La, Pr, Nd). (b) Isothermal magnetization for LnCu$_3$Fe$_4$O$_{12}$ (Ln = La–Lu) measured at 5 K.

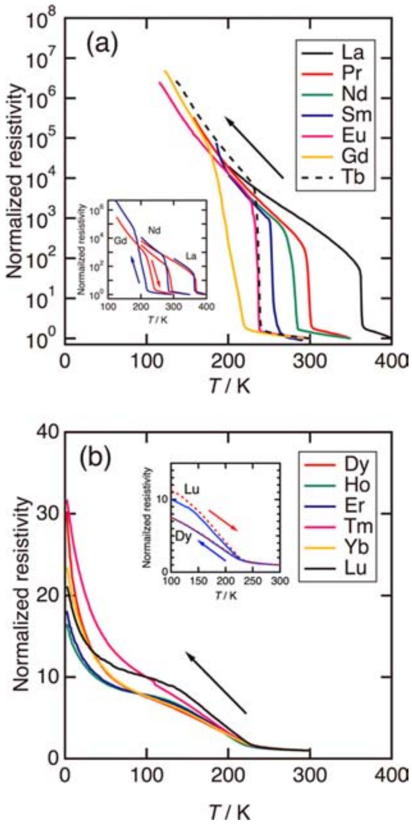

Figure 6. Temperature dependence of the electrical resistivity for LnCu$_3$Fe$_4$O$_{12}$ upon cooling. The resistivity was normalized to the values at 400 K (La), 350 K (Pr, Nd), and 300 K (others). The insets show the thermal hysteresis for Ln = (a) La, Nd, Gd and (b) Dy, Lu.

Figure 6 shows the temperature dependence of the electrical resistivity for LnCu$_3$Fe$_4$O$_{12}$. Metal-to-insulator transitions are observed at temperatures between 220 and 360 K for LnCu$_3$Fe$_4$O$_{12}$ (Ln = La, Pr, Nd, Sm, Eu, Gd, Tb), in which very small temperature dependences of high-temperature metallic phases change into insulator-like large dependences below the CT transition temperature, as reported for LaCu$_3$Fe$_4$O$_{12}$.[26] In contrast, metal-to-semiconductor transitions are observed for LnCu$_3$Fe$_4$O$_{12}$ (Ln = Dy, Ho, Er, Tm, Yb, Lu) below ~220 K (Figure 6b), which are similar to that of YCu$_3$Fe$_4$O$_{12}$ accompanying CD transition. The temperature dependences of the resistivity in the charge-disproportionated phases are much smaller than those in the charge-transferred phases. The inset of Figure 6a shows that a large thermal hysteresis exists in the CT transitions due to their first-order characteristics, while the thermal hysteresis in the CD transitions is negligibly small (see the inset of Figure 6b).

The above analysis of crystal structure, valence states, and physical properties of LnCu$_3$Fe$_4$O$_{12}$ divides these compounds into two classes, in which the first class arouses a CT transition like that of LaCu$_3$Fe$_4$O$_{12}$, and the other class generates a CD transition like that of YCu$_3$Fe$_4$O$_{12}$. In a previous report,[25] we investigated the origin of the alternative electronic phase transitions in A^{3+}Cu$_3$Fe$_4$O$_{12}$ perovskites, concluding that the CT transition predominantly occurs in LaCu$_3$Fe$_4$O$_{12}$ to relieve the bond strains represented as overbonding (underbonding) in the La–O (Fe–O) bond, while the CD transition occurs in YCu$_3$Fe$_4$O$_{12}$ because the opposite kind of bond strains, which are dominant in YCu$_3$Fe$_4$O$_{12}$, are not necessarily relaxed by the CT transition. Here, we attempt to make further refinements to the above conclusions based on the structural data of LnCu$_3$Fe$_4$O$_{12}$. Figure 7a shows selected bond lengths and bond angle versus ionic radius of Ln ions for the Ln^{3+}Cu$^{2+}_3$Fe$^{3.75+}_4$O$_{12}$ phase in the vicinity of room temperature. The Ln–O bond shrinks almost monotonically as the r_{Ln} decreases. The Fe–O bond shrinks correspondingly, while the Cu–O bond length is almost constant. This is because the larger Ln ions expand the unit cell volumes and the Fe–O bonds are accordingly stretched in the relationship $a = 4l_{\text{Fe–O}} \times \sin(\psi/2)$, where a is the lattice constant, $l_{\text{Fe–O}}$ is the Fe–O bond length, and ψ is the Fe–O–Fe bond angle. The Fe–O–Fe bond angle slightly increases with decreasing r_{Ln}, which is attributed to the decrement in the difference in ionic radii between A-site (r_A) and A'-site ($r_{A'}$) ions, Δr_A ($\Delta r_\text{A} = r_A - r_{A'}$), as demonstrated in our previous paper.[38] When Δr_A decreases from 0.59 Å (La) to 0.407 Å (Lu), the Fe–O–Fe bond angle is seen to increase from 139.2 to 140.3°.

The BVS analysis unveils the delicate relationship between Ln–O and Fe–O bonds. Figure 7b shows the BVS, bond discrepancy, and GII in the valence unit (v.u.) as a function of r_{Ln} for the Ln^{3+}Cu$^{2+}_3$Fe$^{3.75+}_4$O$_{12}$ phase. The BVS of Cu is close to the expected value (+2) for all of the compounds, indicating that the Cu–O bond remains in a proper state. On the other hand, the BVS of Ln drastically decreases from +3.60 (La) to

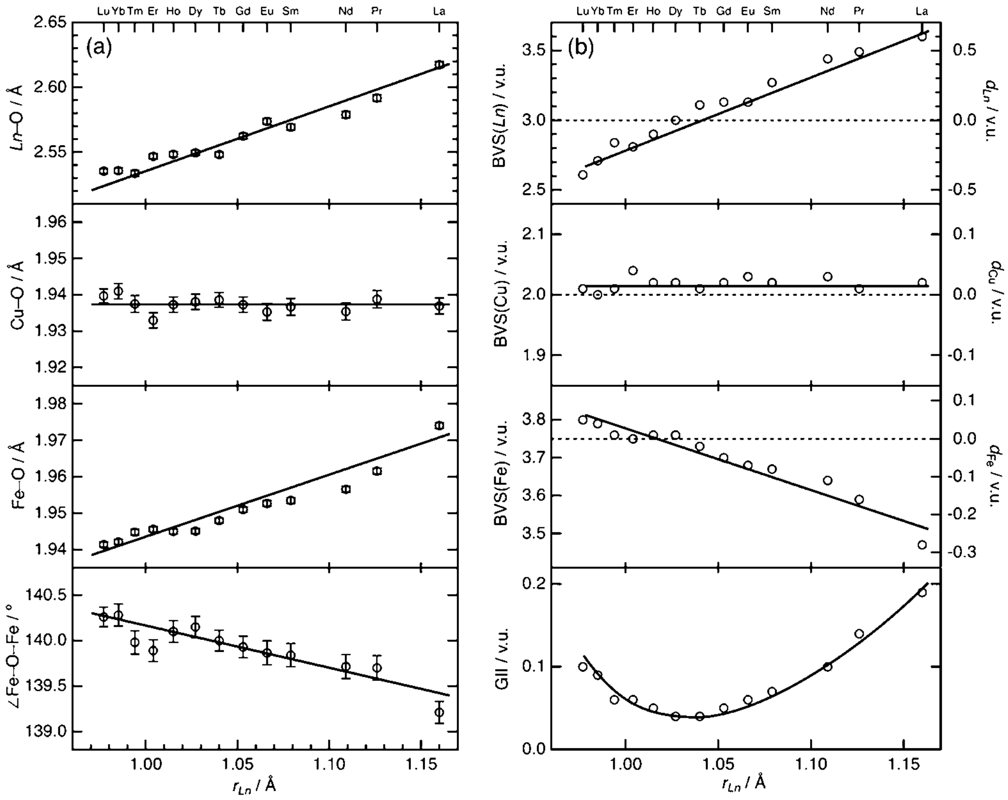

Figure 7. The r_{Ln} dependence of the (a) bond lengths and bond angle, (b) BVS (left axis), GII, and bond discrepancy (right axis). The data for $Ln^{3+}Cu^{2+}{}_3Fe^{3.75+}{}_4O_{12}$ near the room temperature are adopted, using the 400 K data for $LaCu_3Fe_4O_{12}$, 350 K for $PrCu_3Fe_4O_{12}$, and 300 K for the others. The r_{Ln} values in the eight-coordination (CN=8) are adopted.[31] The lines and curve are guides for the eye.

+2.61 (Lu) while the BVS of Fe increases from +3.47 (La) to +3.80 (Lu). Deviations of the BVS from the nominal ionic valences are represented as overbonding or underbonding in the relevant bonds. The overbonding (underbonding) in the *Ln*—O (Fe—O) bond is enhanced from $DyCu_3Fe_4O_{12}$ to $LaCu_3Fe_4O_{12}$. In contrast, the underbonding (overbonding) in the *Ln*—O (Fe—O) bond is enhanced from $DyCu_3Fe_4O_{12}$ to $LuCu_3Fe_4O_{12}$. These trends are considered to be the result of bond strains, which represent structural instability. The instability of each bond is evaluated by the bond discrepancy, d_M, which is defined as $d_M = \mathrm{BVS}(M) - V_M$, where BVS($M$) and V_M are the BVS and ionic valence of the M ion, respectively. The total instability of the structure is evaluated by GII, which is defined as $\mathrm{GII} = [\Sigma_M(d_M{}^2)/N]^{1/2}$, where N is the number of atoms in the formula unit. When the GII increases, the relevant structure becomes unstable. The GII displays a quadric-like dependence on r_{Ln} with the minimum (GII = 0.04 v.u.) found around $DyCu_3Fe_4O_{12}$ (Figure 7b). Note that there exists a pair of the $LnCu_3Fe_4O_{12}$ that have almost the same GII values at the La- and Lu-sides (i.e., GII = 0.06 v.u. for $EuCu_3Fe_4O_{12}$ and $TmCu_3Fe_4O_{12}$, GII = 0.10 v.u. for $NdCu_3Fe_4O_{12}$ and $LuCu_3Fe_4O_{12}$), but the members of this pair transform into opposite types of the electronic phases (CT or CD). A further notable feature is that the CT transition temperature is strongly dependent upon the GII value, as shown in Figure 8a, whereas the CD transition temperature is almost constant in any of the $LnCu_3Fe_4O_{12}$ compounds. This suggests that the thermodynamic stability of the high-temperature $Ln^{3+}Cu^{2+}{}_3Fe^{3.75+}{}_4O_{12}$ phase is sensitive to the bond strains in the case of the CT transitions. In-depth bond strain analysis is conducted in a diagram of d_{Ln} versus d_{Fe} (Figure 8b). $DyCu_3Fe_4O_{12}$ is located at the nearest point to the origin, indicating that this compound has the least amount of bond strain, and thus should transform to an essential electronic ground state of $LnCu_3Fe_4O_{12}$. All of the compounds that generate CT transitions (*Ln* = La, Pr, Nd, Sm, Eu, Gd, Tb) are found in the second quadrant ($d_{Ln} \geq 0$ and $d_{Fe} \leq 0$), while those arousing CD transitions (*Ln* = Dy, Ho, Er, Tm, Yb, Lu) are in the fourth quadrant ($d_{Ln} \leq 0$ and $d_{Fe} \geq 0$). The vacancy existing in the first and third quadrants demonstrates that the *Ln*—O and Fe—O bonds tightly correlate to each other. Specifically, larger *Ln* ions expand the unit cell volume and stretch the Fe—O bond with the elongation of the *Ln*—O bond constrained by the rigid Fe—O framework, while smaller *Ln* ions contract the unit cell and shrink the Fe—O bond, which is limited by the robustness of the Fe—O bond. This proves that a small difference in the type of bond strain may switch the electronic phase transitions precisely. This is a remarkable example of the structural instabilities being categorized by bond discrepancy.

Figure 9 shows the electronic phase diagram for $LnCu_3Fe_4O_{12}$. In this phase diagram, the CT and CD transition temperatures are plotted as a function of r_{Ln}. At high temperature, the paramagnetic metallic phase (PM-M) is dominant for all. $LnCu_3Fe_4O_{12}$ with larger *Ln* ions (*Ln* = La, Pr, Nd, Sm, Eu, Gd, Tb) transform to charge-transferred, antiferromagnetic, and insulating phase (AFM-I), in which the transition temperature decreases with the *Ln* ion radius. In contrast, $LnCu_3Fe_4O_{12}$ with smaller *Ln* ions (*Ln* = Dy, Ho, Er, Tm, Yb, Lu) transform to the charge-disproportionated, ferrimagnetic, and semiconducting phase (FerriM-S), in which the transition temperatures are almost constant. The

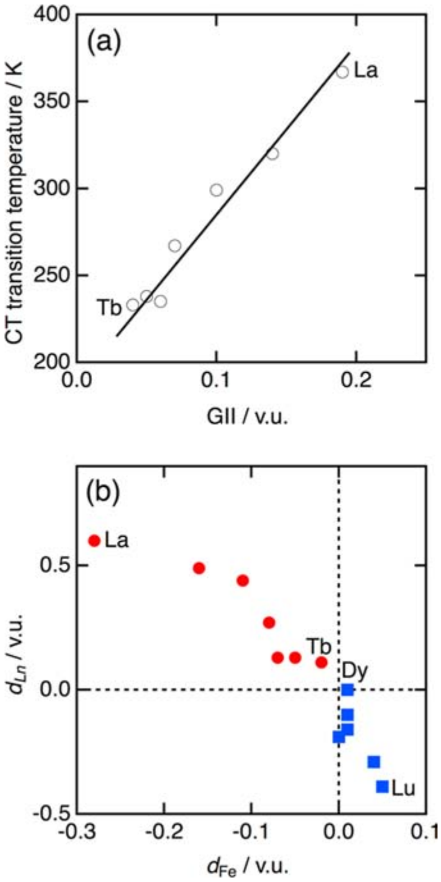

Figure 8. (a) CT transition temperature versus GII for $Ln\text{Cu}_3\text{Fe}_4\text{O}_{12}$ (Ln = La, Pr, Nd, Sm, Eu, Gd, Tb). The GII values are adopted at 400 K for $\text{LaCu}_3\text{Fe}_4\text{O}_{12}$, 350 K for $\text{PrCu}_3\text{Fe}_4\text{O}_{12}$, and 300 K for the other $Ln\text{Cu}_3\text{Fe}_4\text{O}_{12}$ (Ln = Nd, Sm, Eu, Gd, Tb). The line is a guide for the eye. (b) Correlation between d_{Ln} and d_{Fe}. The data are adopted for that at 400 K for Ln = La, 350 K for Ln = Pr, and 300 K for Ln = Nd, Sm, Eu, Gd, Tb, Dy, Ho, Er, Tm, Yb, Lu. Red (blue) markers represent the compounds transforming to CT (CD) phase at low temperature.

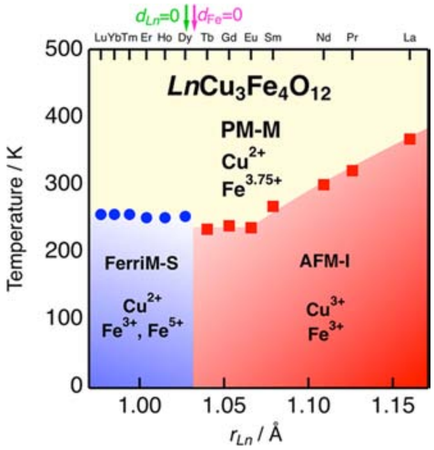

Figure 9. Electronic phase diagram for $Ln\text{Cu}_3\text{Fe}_4\text{O}_{12}$. Red squares (blue circles) represent the CT (CD) transition temperatures, which were determined by XRD data for Ln = La, Pr, Nd, Sm, Eu, Gd, Tb, and ferromagnetic transitions for Ln = Dy, Ho, Er, Tm, Yb, Lu. The PM-M, FerriM-S, and AFM-I regions represent the paramagnetic-metal, ferrimagnetic-semiconductor, and antiferromagnetic-insulator phases, respectively.

electronic phase boundary between AFM-I and FerriM-S is located between $\text{TbCu}_3\text{Fe}_4\text{O}_{12}$ and $\text{DyCu}_3\text{Fe}_4\text{O}_{12}$. This boundary may be interpreted as the "zero-point" of the bond strains, in which no strains are included in any metal−oxygen bonds. This is in sharp contrast to the electronic phase diagram of $\text{Ca}_{1-x}\text{La}_x\text{Cu}_3\text{Fe}_4\text{O}_{12}$ proposed by Chen.[39] In the $\text{Ca}_{1-x}\text{La}_x\text{Cu}_3\text{Fe}_4\text{O}_{12}$ phase diagram, neither local structures nor bond strains were considered, whereas carrier concentration was treated as a primary parameter. In addition, electronic phase separations are unavoidable in a wide range of intermediate compositions. However, our present study successfully reveals that bond strains predominantly control electronic phase transitions of $Ln\text{Cu}_3\text{Fe}_4\text{O}_{12}$ and a clear phase boundary is defined. Therefore, our results enable precise tuning of electronic phases by bond strains, instead of by carrier concentration.

4. CONCLUSIONS

We investigated low-temperature electronic phases of $Ln\text{Cu}_3\text{Fe}_4\text{O}_{12}$ (Ln: lanthanide) perovskites. All of the compounds are in an identical valence state of $Ln^{3+}\text{Cu}^{2+}{}_3\text{Fe}^{3.75+}{}_4\text{O}_{12}$ at high temperature. The compounds with larger Ln ions (Ln = La, Pr, Nd, Sm, Eu, Gd, Tb) induce an intersite charge transfer ($3\text{Cu}^{2+} + 4\text{Fe}^{3.75+} \rightarrow 3\text{Cu}^{3+} + 4\text{Fe}^{3+}$) at temperatures between 240 and 360 K, whereas all compounds with smaller Ln ions (Ln = Dy, Ho, Er, Tm Yb, Lu) generate a charge disproportionation ($8\text{Fe}^{3.75+} \rightarrow 5\text{Fe}^{3+} + 3\text{Fe}^{5+}$) below ~250−260 K. The former series exhibits metal-to-insulator, antiferromagnetic, and isostructural volume expansion transitions simultaneously with the intersite charge transfer. In contrast, the latter shows metal-to-semiconductor, ferrimagnetic, and charge ordering transitions simultaneously with the charge disproportionation. Structural instability of $Ln\text{Cu}_3\text{Fe}_4\text{O}_{12}$ as estimated from the bond discrepancies and global instability indices demonstrate that the bond strains in these compounds are distinguished into two types, which are well illustrated in a bond strain diagram. The first type is overbonding in the Ln−O bond and underbonding in the Fe−O bond, while the other type is the opposite. Intersite charge transfer transition temperatures are dependent upon the global instability indices, whereas those of the charge disproportionation transition are almost identical regardless of the magnitude of structural instability. Our bond strain analysis demonstrates that the bond strains may control the electronic phase transitions precisely.

■ ASSOCIATED CONTENT

Ⓢ Supporting Information

XRD patterns, SXRD patterns, ED patterns, MCD spectra, and crystallographic data (CIF) for $Ln\text{Cu}_3\text{Fe}_4\text{O}_{12}$. This material is available free of charge via the Internet at http://pubs.acs.org.

■ AUTHOR INFORMATION

Corresponding Author

*E-mail: i-yamada@21c.osakafu-u.ac.jp

Present Address

[†]Deutsches Elektronen Synchrotron (DESY), 22607 Hamburg, Germany

Notes

The authors declare no competing financial interest.

■ ACKNOWLEDGMENTS

We thank Shintaro Ishiwata for helpful discussion, and Hiroshi Kageyama, Minoru Nohara, and Kensuke Konishi for support in the acquisition of magnetization data. We also thank Shigeki Mori for preliminary measurements of temperature-variable XRD patterns. The synchrotron radiation experiments were performed at SPring-8 with the approval of JASRI (Proposal Nos. 2010B1707, 2011A1047, 2012A1002, 2012A1619, 2013A1042, 2013A1043, and 2013A1689). Parts of this work were performed using the facilities of ISSP. This work was partially supported by the Murata Science Foundation.

■ REFERENCES

(1) Imada, M.; Fujimori, A.; Tokura, Y. *Rev. Mod. Phys.* **1998**, *70*, 1039.

(2) Brown, I. D.; Altermatt, D. *Acta Crystallogr., Sect. B* **1985**, *41*, 244.

(3) Brown, I. D. *Chem. Rev.* **2009**, *109*, 6858.

(4) Lufaso, M. W.; Woodward, P. M. *Acta Crystallogr., Sect. B* **2001**, *57*, 725.

(5) Alonso, J. A.; Martinez-Lope, M. J.; de la Calle, C.; Pomjakushin, V. *J. Mater. Chem.* **2006**, *16*, 1555.

(6) Zhang, H.; Li, N.; Li, K.; Xue, D. F. *Acta Crystallogr., Sect. B* **2007**, *63*, 812.

(7) MacChesney, J. B.; Sherwood, R. C.; Potter, J. F. *J. Chem. Phys.* **1965**, *43*, 1907.

(8) Takeda, T.; Yamaguchi, Y.; Watanabe, H. *J. Phys. Soc. Jpn.* **1972**, *4*, 967.

(9) Ishiwata, S.; Tokunaga, M.; Kaneko, Y.; Okuyama, D.; Tokunaga, Y.; Wakimoto, S.; Kakurai, K.; Arima, T.; Taguchi, Y.; Tokura, Y. *Phys. Rev. B* **2011**, *84*, 060406(R).

(10) Bocquet, A. E.; Fujimori, A.; Mizokawa, T.; Saitoh, T.; Namatame, H.; Suga, S.; Kimizuka, N.; Takeda, Y.; Takano, M. *Phys. Rev. B* **1992**, *45*, 1561.

(11) Bocquet, A. E.; Mizokawa, T.; Saitoh, T.; Namatame, H.; Fujimori, A. *Phys. Rev. B* **1992**, *46*, 3771.

(12) Takano, M.; Nakanishi, N.; Takeda, Y.; Naka, S.; Takada, T. *Mater. Res. Bull.* **1977**, *12*, 923.

(13) Mostovoy, M. *Phys. Rev. Lett.* **2005**, *94*, 137205.

(14) Hayashi, N.; Yamamoto, T.; Kageyama, H.; Nishi, M.; Watanabe, Y.; Kawakami, T.; Matsushita, Y.; Fujimori, A.; Takano, M. *Angew. Chem., Int. Ed.* **2011**, *50*, 12547.

(15) Li, Z.; Laskowski, R.; Iitaka, T.; Tohyama, T. *Phys. Rev. B* **2012**, *85*, 134419 .

(16) Alonso, J. A.; Sanchez-Benitez, J.; De Andres, A.; Martinez-Lope, M. J.; Casais, M. T.; Martinez, J. L. *Appl. Phys. Lett.* **2003**, *83*, 2623.

(17) Zeng, Z.; Greenblatt, M.; Subramanian, M. A.; Croft, M. *Phys. Rev. Lett.* **1999**, *82*, 3164.

(18) Kobayashi, W.; Terasaki, I.; Takeya, J.; Tsukada, I.; Ando, Y. *J. Phys. Soc. Jpn.* **2004**, *73*, 2373.

(19) Prodi, A.; Gilioli, E.; Gauzzi, A.; Licci, F.; Marezio, M.; Bolzoni, F.; Huang, Q.; Santoro, A.; Lynn, J. W. *Nat. Mater.* **2004**, *3*, 48.

(20) Subramanian, M. A.; Li, D.; Duan, N.; Reisner, B. A.; Sleight, A. W. *J. Solid State Chem.* **2000**, *151*, 323.

(21) Akizuki, Y.; Yamada, I.; Fujita, K.; Nishiyama, N.; Irifune, T.; Yajima, T.; Kageyama, H.; Tanaka, K. *Inorg. Chem.* **2013**, *52*, 11538.

(22) Ovsyannikov, S. V.; Abakumov, A. M.; Tsirlin, A. A.; Schnelle, W.; Egoavil, R.; Verbeeck, J.; Van Tendeloo, G.; Glazyrin, K. V.; Hanfland, M.; Dubrovinsky, L. *Angew. Chem., Int. Ed.* **2013**, *52*, 1494.

(23) Yamada, I.; Takata, K.; Hayashi, N.; Shinohara, S.; Azuma, M.; Mori, S.; Muranaka, S.; Shimakawa, Y.; Takano, M. *Angew. Chem., Int. Ed.* **2008**, *47*, 7032.

(24) Yamada, I.; Tsuchida, K.; Ohgushi, K.; Hayashi, N.; Kim, J.; Tsuji, N.; Takahashi, R.; Matsushita, M.; Nishiyama, N.; Inoue, T.; Irifune, T.; Kato, K.; Takata, M.; Takano, M. *Angew. Chem., Int. Ed.* **2011**, *50*, 6579.

(25) Etani, H.; Yamada, I.; Ohgushi, K.; Hayashi, N.; Kusano, Y.; Mizumaki, M.; Kim, J.; Tsuji, N.; Takahashi, R.; Nishiyama, N.; Inoue, T.; Irifune, T.; Takano, M. *J. Am. Chem. Soc.* **2013**, *135*, 6100.

(26) Long, Y. W.; Hayashi, N.; Saito, T.; Azuma, M.; Muranaka, S.; Shimakawa, Y. *Nature* **2009**, *458*, 60.

(27) Long, Y. W.; Saito, T.; Tohyama, T.; Oka, K.; Azuma, M.; Shimakawa, Y. *Inorg. Chem.* **2009**, *48*, 8489.

(28) Dittl, A.; Krohns, S.; Sebald, J.; Schrettle, F.; Hemmida, M.; von Nidda, H. A. K.; Riegg, S.; Reller, A.; Ebbinghaus, S. G.; Loidl, A. *Eur. Phys. J. B* **2011**, *79*, 391.

(29) Sanchez-Benitez, J.; Alonso, J. A.; Falcon, H.; Martinez-Lope, M. J.; De Andres, A.; Fernandez-Diaz, M. T. *J. Phys.: Condens. Matter* **2005**, *17*, S3063.

(30) Brown, I. D. *The Chemical Bond in Inorganic Chemistry*; Oxford University Press: Oxford, UK, 2001.

(31) Shannon, R. D. *Acta Crystallogr., Sect. A* **1976**, *32*, 751.

(32) Kakihana, M. *J. Sol.-Gel Sci. Technol.* **1996**, *6*, 7.

(33) Izumi, F.; Momma, K. *Solid State Phenom.* **2007**, *130*, 15.

(34) Momma, K.; Izumi, F. *J. Appl. Crystallogr.* **2011**, *44*, 1272.

(35) Long, Y. W.; Shimakawa, Y. *New J. Phys.* **2010**, *12*, 063029.

(36) Mizokawa, T.; Fujimori, A.; Namatame, H.; Takeda, Y.; Takano, M. *Phys. Rev. B* **1998**, *57*, 9550.

(37) McGuinness, C.; Downes, J. E.; Sheridan, P.; Glans, P. A.; Smith, K. E.; Si, W.; Johnson, P. D. *Phys. Rev. B* **2005**, *71*, 195111.

(38) Shiro, K.; Yamada, I.; Ikeda, N.; Ohgushi, K.; Mizumaki, M.; Takahashi, R.; Nishiyama, N.; Inoue, T.; Irifune, T. *Inorg. Chem.* **2013**, *52*, 1604.

(39) Chen, W.; Saito, T.; Hayashi, N.; Takano, M.; Shimakawa, Y. *Sci. Rep* **2012**, *2*, 449.

(40) Woodward, P. M.; Cox, D. E.; Moshopoulou, E.; Sleight, A. W.; Morimoto, S. *Phys. Rev. B* **2000**, *62*, 844.

(41) Kanowitz, S. M.; Palenik, G. J. *Inorg. Chem.* **1998**, *37*, 2086.